Third International Conference on CFD in the Minerals and Process Industries
CSIRO, Melbourne, Australia
10-12 December 2003

EXPERIMENTAL AND NUMERICAL STUDY OF THE COLD CRUCIBLE MELTING PROCESS

K PERICLEOUS[1], V BOJAREVICS[1], RA HARDING[2], M WICKINS[2]

[1]University of Greenwich, School of Computing and Mathematics, UK
[2] University of Birmingham IRC in Materials Processing, UK

ABSTRACT

The Cold Crucible, or Induction Skull Melting process as is otherwise known, has the potential to produce high purity melts of a range of difficult to melt materials, including Ti-Al alloys for Aerospace, Ti-Ta and other biocompatible materials for implants, Silicon for photovoltaic and electronic applications, etc. Induction currents melt the alloy in the crucible and partially suspend it away from water-cooled surfaces.

Strong stirring takes place in the melt due to electromagnetic forces and very high temperatures are attainable under the right conditions. In a joint numerical and experimental research programme, various aspects of the design and operation of this process are investigated to increase our understanding of the physical mechanisms involved and to maximise efficiency. A combination of FV and Spectral CFD techniques are used at Greenwich to tackle this problem with the experimental work taking place at Birmingham University. Results of this study presented here, highlight the effects of turbulence and free surface behaviour on attained superheat and also discuss coil design variations and dual frequency options that may lead to winning designs.

NOMENCLATURE

$\boldsymbol{A}$ magnetic field vector potential
$\boldsymbol{B}$ magnetic field density
C_p specific heat
$\boldsymbol{f}$ Lorentz force vector
$\boldsymbol{g}$ gravity vector
H_{ch} heat transfer coefficient
I RMS coil current
$\mathbf{J}$ current density
k is the kinetic energy of turbulence per unit mass
p pressure
r radius from conductor
u,v velocity components
$\mathbf{v}$ velocity vector
V voltage
T temperature
t time

α thermal diffusivity
ε emissivity
n kinematic viscosity
ρ density
σ electrical conductivity
σ_B Boltzman constant.
ω vorticity fluctuation frequency or, induction current angular frequency

INTRODUCTION

There has been an extensive worldwide research effort to develop gamma titanium aluminide (γ-TiAl) alloys for use in high performance components such as turbine blades, exhaust valves and turbocharger rotors. Small-scale production of certain components has started [1, 2] but there are various technological and economic barriers to more widespread production. Part of the ongoing research is aimed at developing more effective means of melting and casting these alloys, with particular emphasis on the Induction Skull Melting (ISM) process. In this, the metal is held in a water-cooled copper crucible and melted with a high power induction field, Figure 1. In this arrangement, much of the input energy is lost to the crucible, resulting in poor energy efficiency, but also a low superheat which in turn causes a number of casting problems: incompletely filled moulds (misruns) macro-porosity and entrained bubble defects. It is recognised that careful experiments coupled with CFD modelling is crucial in understanding and improving this process.

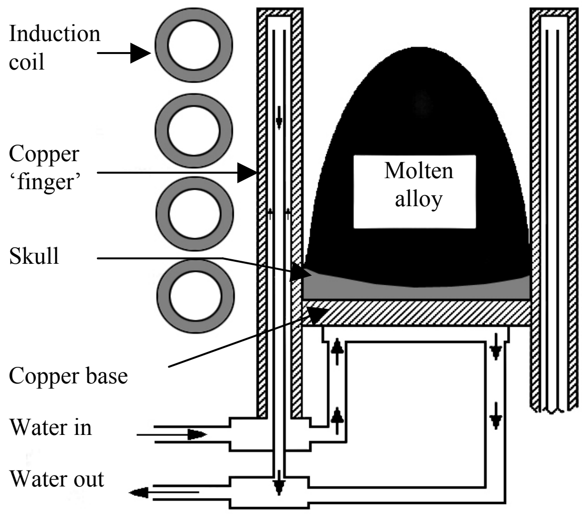

Figure 1: An ISM cold crucible (schematic).

Current research at the University of Birmingham [3] is developing practical ways of improving the quality of TiAl investment castings in close collaboration with the University of Greenwich where a comprehensive computer model of an ISM furnace is being developed [4, 5] using a combination of spectral and finite-volume CFD techniques. For realism, accurate thermophysical and electrical property data are required to run the model. Obtaining such data is a challenge in itself, because TiAl alloys are very reactive in the molten condition. Some data are now available [6] for the Ti-44Al-8Nb-1B alloy of particular interest. The experimental programme described in this paper concerns the additional technological data required for input into the model and for validation. These include the true current in the induction coil, the heat flow to the crucible coolant and the shape of the molten metal meniscus.

NUMERICAL MODEL DESCRIPTION

The modelling challenge

The governing equations must represent several coupled phenomena: turbulent fluid flow in the melt, heat transfer and phase-change, and electromagnetic interactions between the induction coil, the crucible and the conducting metal charge within it. The additional challenge here, which makes this a formidable problem to solve, concerns the time-dependent variation in the melt geometry. The instantaneous melt shape is a balance of gravity, electromagnetic force, surface tension and fluid inertia forces. Since changes in geometry have a direct influence on the electromagnetic field, no form of uncoupling is possible.

Since the crucible is cylindrical, axisymmetry can be assumed. However, localised 3D effects become important, especially where the molten metal bridges the crucible segments leading to a "short-circuiting" effect [7]. It has been necessary to use both 3D FV and axisymmetric spectral methods in this work.

Due to the high frequency (~7kHz) employed in the induction coil, electromagnetic effects are dominant in a thin boundary layer region on the surface of the melt. A fine grid is needed in this region and this grid must follow the oscillations of the surface. A grid transformation procedure was developed for this reason (see [8] for details).

Governing Equations

The thermofluid problem is represented by the time-dependent Navier-Stokes and continuity equations, plus the heat transfer equations for the fluid and solid zones of the metal charge:

$$\begin{aligned} &\partial_t \mathbf{v} + (\mathbf{v}\cdot\nabla)\mathbf{v} - \nabla\cdot(\nu_e(\nabla\mathbf{v} + \nabla\mathbf{v}^T)) = \\ &-\rho^{-1}(\nabla p \ \text{-K}_\text{D}\mathbf{v} + \mathbf{f}) + \mathbf{g} \end{aligned} \qquad (1)$$

$$\nabla\cdot(\rho\mathbf{v}) = 0 \qquad (2)$$

$$C_p^*(\partial_t T + \mathbf{v}\cdot\nabla T) = \nabla\cdot(C_p\alpha_e\nabla T) + \frac{|\mathbf{J}|^2}{\rho\sigma} \qquad (3)$$

where $\nu_e = \nu_T + \nu$ is the effective viscosity (sum of turbulent and laminar viscosity), $-K_D \mathbf{v}$ is a Darcy term representing the mushy zone and melting front modelling, $\alpha_e = \alpha_T + \alpha$ is the effective thermal diffusivity, C_p^* - the solid-fraction-modified specific heat function that accounts for latent heat effects (see [8] for details), and $|\mathbf{J}|^2/\sigma$ is the Joule heat. The dynamic fluid flow problem is solved with the full set of instantaneous boundary conditions: at the liquid metal free surface normal hydrodynamic stress is compensated by the surface tension and the tangential stress is zero. A kinematic condition, ensures the free surface location (and the grid) moves with the fluid material particles. A no-slip condition is applied to the velocity where there is a contact at solid walls at any instant. The free surface contact position against the crucible "fingers" is very important for heat transfer. It moves in accordance with force balance and the kinematic conditions.

Temperature boundary conditions are expressed as thermal fluxes to the surroundings: radiation and the effective turbulent heat transfer at solid walls. Hence [9], with the empirical heat transfer coefficient H_{ch} *(T)*:

$$-\rho C_p\alpha_e\ \partial_n\ T = H_{ch}(T)\cdot(T - T_w) \qquad (4)$$

where T_w is wall temperature. The data for H_{ch} *(T)* [$Wm^{-2}K^{-1}$] are obtained from comparisons with experimentally measured heat losses to the water cooled walls as described below. With reference to the temperature T at the wall contact position (T_S – solidus temperature, T_L – liquidus temperature):

$$\begin{aligned} &H_{ch} = 110 \ \text{, if } T < T_S \text{, and} \\ &H_{ch} = 110 + (T - T_S)*100 \ \text{, if } T \geq T_S. \end{aligned} \qquad (5)$$

At the free surface the radiation condition is used:

$$-\rho C_p\alpha_e\ \partial_n\ T = \varepsilon\sigma_B(T^4 - T_w^4) \qquad (6)$$

where the emissivity ε = 0.3 according to available data.

The fluid flow is turbulent, and the 2-equation *k-ω* time-dependent turbulence model [10] is used to compute the effective viscosity and turbulent heat transport. The temperature boundary conditions depend on the local effective thermal diffusion coefficient α_e at the wall and the free surface, which is proportional to the effective turbulent viscosity ν_e. The appropriate *k-ω* model is the low Re number version which resolves the flow from laminar to fully developed turbulent states, and therefore it is suitable for the flow within the slow mushy zones and the bulk of the fully molten liquid metal at the final mixing stages. The computation follows in detail the time development of the turbulent characteristics determined by the coupled non-linear transport equations accounting for a continuous generation and destruction of the turbulent energy.

An axisymmetric pseudo-spectral spatial representation is used for equations (1-3), and also the *k-ω* model equations. Typically an overnight turnover time results for each case computed. For efficiency, implicit time stepping (typically Δt = 0.1 - 4 ms) with iterative linearisation of the non-linear terms is used[8].

The electromagnetic field

The computational procedure for the electromagnetic field is implemented on the same grid as the fluid equations. An exponentially dense Chebyshev grid distribution is used to ensure high resolution within the surface boundary layer.

The electromagnetic force f for the axisymmetric situation is computed using a fast mutual inductance algorithm based on a Biot-Savard integral [8]. In addition, the 3D FV code PHYSICA[11] has been used to compute the electric current distribution within the segmented copper wall fingers. For this purpose PHYSICA was adapted for sinusoidal electric current ($J = J(r)e^{i\omega t}$) to solve the equation:

$$\nabla\times(\nabla\times\mathbf{J}) + i\omega\mu_0\sigma\ \mathbf{J} = 0 \qquad (8)$$

with the boundary conditions of zero normal electric current at non-conducting walls, $J_n(\mathbf{r_S}) = 0$, and tangential components that are given by the equation *rot* (**J**) = $i\omega\sigma$ $\mathbf{B}(\mathbf{r_S})$. The magnetic field **B** at the boundaries is determined by integrating the Biot-Savart law over all the current-carrying regions. An example of the calculated electric current distribution within the mid-section of the wall fingers is shown in Figure 2, where it is evident that the radial electric currents along the adjoining fingers gap are in opposite directions and equal in magnitude; this justifies a 'quasi-axisymmetric' approximation when computing the magnetic field produced by the fingers outside of their volume. The axisymmetric integral equation based algorithm updates the effective current path within the fingers from the 3D solution, i.e., increased by the radial part and located within the skin layer depth according to the solution. The details of this procedure are particularly important when determining the Joule heat directly released in the copper fingers which is a significant part of the total energy losses within the cold crucible.

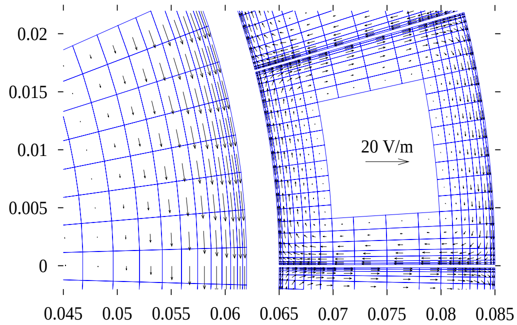

Figure 2: The calculated electric current distribution within the mid-section of the copper wall fingers. Only one of the fingers (from the total of 24) is shown, the others are periodic to the shown distribution.

In the axisymmetric case, the current averaged over the AC supply period is given by Ohm's law for moving media:

$$\mathbf{J} = \sigma(-\partial_t \mathbf{A} + \mathbf{v} \times \mathbf{B}) = \mathbf{J}_{AC} + \mathbf{J}_{\mathrm{v}} \quad (9)$$

Where, $\mathbf{J}_{AC}$ is induced in the conducting medium with the assumption of zero velocity. The same elliptic integral representation can be used to represent the DC magnetic field created by an additional external coil. The solution in the liquid volume depends on its free surface shape and needs to be recomputed when the shape changes. The resulting electromagnetic force **f**, time-averaged over the AC period, can be decomposed in two parts:

$$\mathbf{f} = \mathbf{f}_{\mathrm{AC}} + \mathbf{f}_{\mathrm{v}} \quad (10)$$

where the second, is the fluid-velocity-dependent part. The magnetic field components may include AC and DC parts, both of which contribute to the time-averaged force.

EXPERIMENTAL PROCEDURES

Melting Furnace

An ISM furnace of nominal melting capacity ~4.5 kg TiAl was used. This is located inside a chamber to allow melting to be carried out under vacuum or a partial argon pressure. The induction coil is connected to a VIP power supply with a nominal 350 kW at ~7 kHz. Melting usually involves stepping up the power with time: 50 kW is applied initially and the power then ramped up to 200 kW to achieve melting and then to 350 kW for a short time to maximise superheat in the metal charge without overheating the cooling water. The VIP provides constant power output but the instrumentation does not indicate the current in the coil. Knowledge of the latter is an essential input into the model.

Induction coil current calibration

Calibrations have been established to relate the actual current in the induction coil to the nominal melting power displayed by a kW meter on the control desk, and the effects of the melting stock and its temperature and phase have been assessed. The power supply is connected to the coil via busbars, flexible leads and a coaxial port which feeds the power through the wall of the vacuum vessel and allows the crucible to be tilted. The current was measured outside the vacuum chamber using a current transformer (CT) designed to work at frequencies up to 10 kHz and a current ratio of 8000:5 (i.e. 1600 amps in the power leads gave 1 amp output from the CT). A calibrated, watercooled 1 ohm resistor was connected in parallel with the CT and the voltage across it was measured with an oscilloscope. The RMS coil current, I_c, was given by:

$$I_c = (8000/5)\ V/(2R\sqrt{2}) \text{ amps} \quad (11)$$

V is the peak-to-trough voltage and R the actual value of the resistance. The operating frequency was measured by aligning cursors on the oscilloscope screen with two successive peaks and was displayed automatically.

Temperature measurements

Figure 3 shows a schematic of the cooling circuit. De-ionised water containing ~25% monoethylene glycol (MEG) antifreeze is pumped from a buffer tank into a manifold in the crucible base and is then split into two to cool the base and the fingers, the amount to each being controlled by the crucible design. The water exits from the crucible in two pipes which later join together, then pumped to an air-blast radiator on the roof and finally returned to the buffer tank. The total capacity of the system is estimated to be ~3000 litres. The water was circulated through the system for several hours prior to each run to ensure a uniform initial temperature.

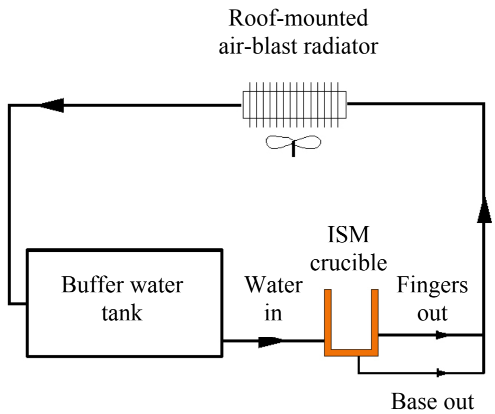

Figure 3: The ISM cooling circuit.

An ultrasonic flow gauge was calibrated for the coolant composition and temperature and used to measure flow in different parts of the circuit. The average flows were 24 l/min through the base and 206 l/min through the fingers (both ±5%). A constant specific heat value of 0.91 cal g^{-1} C^{-1} (3.81 J g^{-1} C^{-1}) was assumed for this work interpolated using the supplier's data.

Calibrated 2 mm-dia, stainless steel sheathed, mineral insulated chromel-alumel thermocouples were validated at

3 temperatures and then inserted into the water pipes to measure the water temperatures. The temperatures were recorded to an accuracy of 0.1˚C every second on a mini TC16 data-logger.

For the Al melts, a metal sheathed chromel-alumel thermocouple was inserted into a hole drilled along the axis of the billet to its half-depth (57 mm) and temperatures recorded on the data-logger. The thermocouple was also used to measure the cooling rate of the billet as it solidified and cooled inside the ISM crucible. Attempts to measure the temperature of the TiAl during or after melting were unreliable due to the limited thermocouple life.

Melting stock

A variety of melting stocks was used:

- Pure (99.99%) aluminium.
- A wrought aluminium alloy (grade 6082T6 to BS1474) containing 0.89% Si, 0.23% Fe, 0.043% Cu, 0.71% Mn, 0.88% Mg, 0.14% Cr, 0.03% Zn, 0.014% Ti, balance Al.
- A nickel alloy (Rolls Royce grade MSRR 7047, equivalent to IN100) of the following specification: 8-11% Cr, 4.5-5% Ti, 5-6% Al, 13-17% Co, 2-4% Mo, 0.7-1.2% V).
- Ti-45Al-8Nb-1B (atomic %) produced as continuously cast billets in the IRC's plasma melting furnace was used for most TiAl melts. TiAl returns were used for some melts.

Melting trials

Coil current calibration: Unless stated otherwise, all melting was done under a partial pressure of 200 mbar of Ar and the power was ramped up in ~50 kW steps (~60 s at each) to a maximum of 350 kW. Regular readings were taken of the voltage across the CT resistor and the VIP power. Once the maximum power had been reached and equilibrium established, the power was reduced in steps and further readings made. At the lower power levels, the metal was barely levitated and started to solidify.

Figure 4 compares the current measured for Al, Ni and TiAl alloys and shows that the calibration curve for the Al alloy was slightly higher than the others. There is a difference between the current drawn with increasing power as opposed to that of decreasing power. This is most likely due to the difference in contact area between the pre-melt ingot which only touches the base and the re-solidified ingot which increasingly also touches the fingers as power is reduced. Considering the different electrical properties of the three alloys, there is surprisingly little difference on the coil current.

Water temperature measurements: Various power-time schedules and furnace atmospheres were used for 7 melts of Al alloy and pure Al and 6 melts of TiAl. It took ~15-20 s to increase the power to a given level, and the power was held constant for long enough to establish pseudo-equilibrium. The applied power was indicated on a digital kW meter but since this has not been calibrated, the measured power levels should be regarded as nominal.

Figure 5 shows typical water and metal temperatures for an Al alloy melted under 200 mbar of argon and then allowed to solidify in the ISM crucible. As the metal reached its melting range (at ~400 s), the rate of temperature rise decreased, then increased and decreased again. The applied power was constant during this time

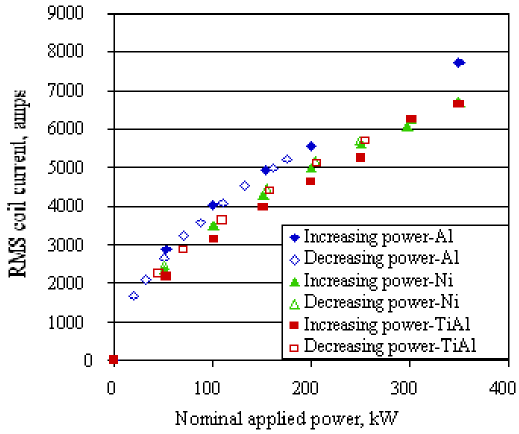

Figure 4: RMS Current comparisons for Al, Ni and TiAl melts

and it is assumed that this change in rate of increase in temperature was due to the absorption of latent heat. Once fully molten, the metal temperature increased slightly when the power was increased at ~535 s, and then decreased again during long term holding. Increasing the power from 150 to 201 kW had no measurable effect on the metal temperature.

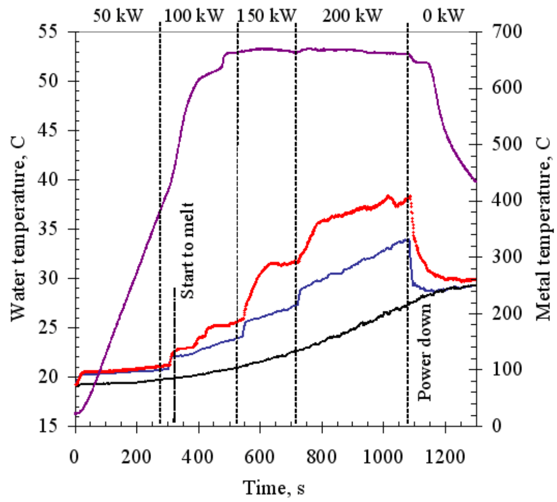

Figure 5: Temperature measurements when melting Al alloy at 200mbar Ar

The inlet water temperature gradually increased throughout the melt and the outlet temperatures from the base and fingers increased noticeably with power. There were several discontinuities in the base water outlet temperature: some of these (at ~400 s) appeared to be related to the billet becoming almost fully molten. The perturbations on the finger outlet trace at ~1000s may be related to melt oscillations and corresponding contact area changes, seen also in the computer simulations.

Meniscus shape Although the progress of melting can be observed through a port, this is almost vertically over the melt and gives a misleading impression of the shape of the molten metal. To validate the model, the height of the centre of molten Ti-44Al-8Nb-1B alloy was measured by inserting a wire probe which melted back to the meniscus surface. The power was then reduced to zero so that the semi-levitated metal collapsed into the ISM crucible and solidified. This then allowed the position of the dome meniscus to be measured relative to the top of the crucible. Measurements were made for different charge weights and melting powers.

Figure 6 shows that, as expected, the dome height relative to the crucible rim increased with increasing melt weight and power. However, it came as a considerable surprise to discover that all of the 4 kg melts protruded above the crucible rim since this was not at all obvious when viewing the melts. This can explain the instability which is sometimes experienced, and undoubtedly affects the superheat achieved in the melt.

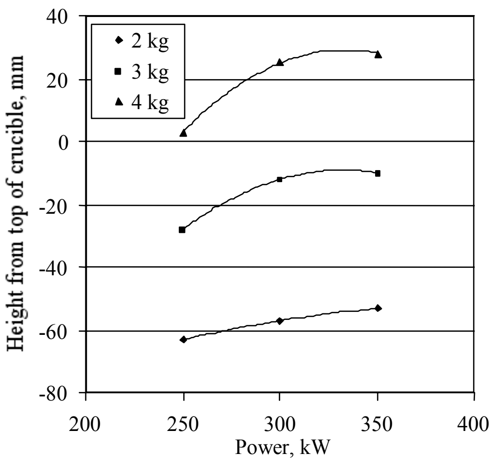

Figure 6: Effect of power and melt weight on dome height for Ti-45Al-8Nb-1B

NUMERICAL RESULTS AND VALIDATION

Figure 7 depicts a typical melt simulation, in this case 2.8kg of Al. The melt is almost complete, with only a small section close to the base remaining solid (shown shaded in the plot). Highest temperature of 672^{o}C is located along the side, although strong mixing induced by the electromagnetic force ensures that the temperature within the liquid phase only varies by about 12 ^{o}C.

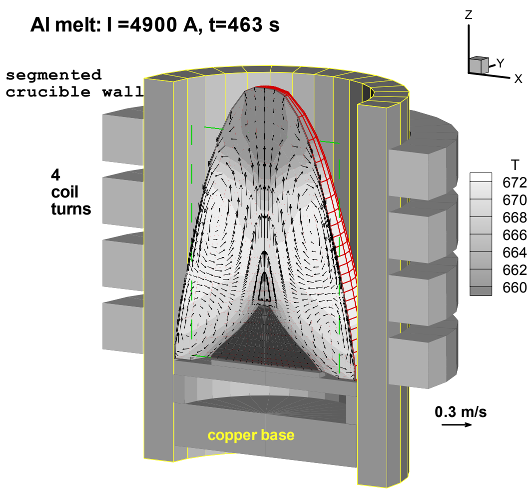

Figure 7: Computed instantaneous dome-shaped Al melt volume, velocity field and temperature distribution (click to animate)

The velocity field is driven by two toroidal vortices, which meet opposite the second coil turn from the base. Maximum velocities (0.3m/s) lie in the thin skin layer, where also the electromagnetic force is at its maximum.

The melting process: The melting sequence is best seen in the accompanying animation (CD version). The ingot is initially solid, so the problem reduces to that of heat conduction only. This initial stage of computation is very fast, since there are no geometrical changes and no fluid flow. Large timesteps (up to 10s) can be used. Melting starts on the side of the ingot and once there is sufficient molten metal the fluid flow and surface deformation procedures switch on, requiring now timesteps of the order of 1ms. The molten metal tends to first fill the space between the ingot and the crucible due to gravity. Since the electromagnetic force (JxB) acts radially inwards on the liquid layer the melt is also forced upwards to cover the top of the ingot.

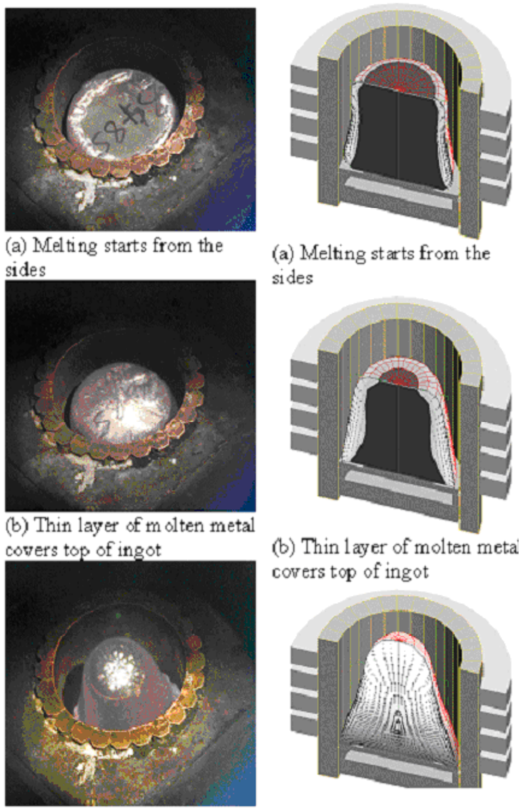

Figure 8: Video stills of the melting sequence and numerical simulations (a) t= 400s, (b) = 450s, (c) t = 600s

As more metal melts, then a dome of liquid is formed, within which strong turbulent convection takes place. For a given volume of metal the height of the dome will increase with induction current as shown by the experiments. In many cases, the dome height exceeds the top of the crucible – since it then also exceeds the top of the coil, induction efficiency reduces. Any further energy input will simply result in higher losses within the copper crucible, manifested as an increase in cooling water temperature. The last place to melt is the bottom of the ingot, which is in continuous contact with the water-cooled base.

This sequence of events, predicted by the computation has been captured on video through the observation port. Aluminium melts in Ar atmosphere provided the best results for visualisation, when a clear view of the melt surface can be maintained during the whole melting cycle. Figure 8 shows side-by-side a series of snapshots and equivalent numerical simulations, presented in a perspective view corresponding to the observation angle.

Dome height validation: Although the qualitative similarity is evident, more quantitative data are necessary to validate the numerical code. Figure 9 shows the measured and free surface height positions for aluminium. The final "steady state" position is well predicted by the simulation at all power levels. Also shown is the onset of oscillations accompanying each step change in power, highlighted by the simulations. Similar agreement has been obtained for TiAl melts and for different melt loads.

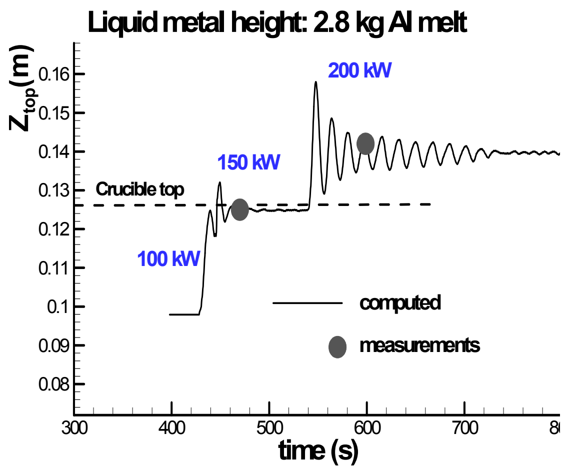

Figure 9: The computed liquid metal top surface position change during the supplied AC field power increase

Power input vs temperature: The water temperature measurements were used to calibrate the unknown heat transfer coefficient in (5). Then the predicted temperatures were compared against experimental measurements as shown in Figure 10.

Temperature first rises in the solid ingot up to the melting temperature, (t~400s) where the temperature remains constant until the melt is complete. Further increase in power only gives a marginal increase in superheat, which reaches a maximum as the losses balance the power input into the metal. The reason for this upper limit in superheat can be inferred from the bottom two plots in the figure, representing power dissipation in the base and the fingers. As the power input increases from 150kW to 200kW, so do the losses; ~70% of the input is wasted in increasing the cooling water temperature. Once the power is switched off, the temperature maintains a second plateau as the metal solidifies. Beyond 1000s, the temperature decreases monotonically in the now solid charge. Throughout this history, the simulations follow quite closely the experiments. The small oscillations in the base power output between 400-500s, coincide with the initial filling of the perimeter gap between the ingot and the crucible wall; some difference between experiment and simulation is observed here.

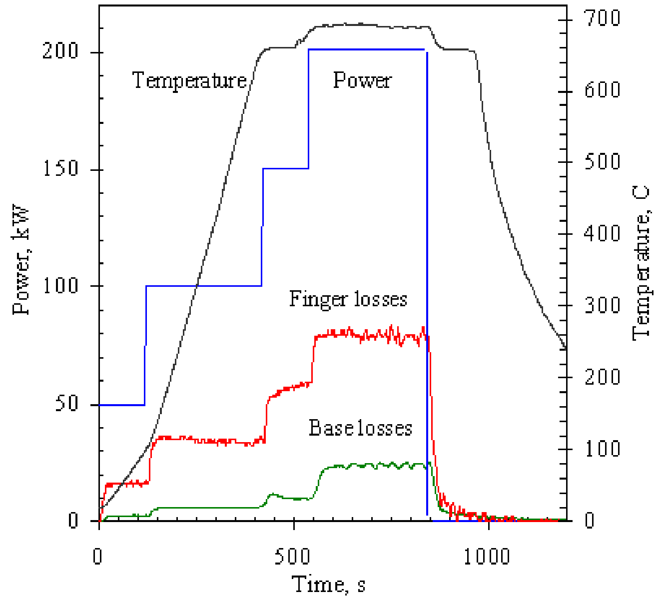

Figure 10: Measured (dashed) vs. predicted temperature history and power distribution during a typical melt cycle – power input in steps; melting starts at ~400s , power off at 850s

The role of turbulence: One of the main factors affecting heat transfer, hence superheat, is turbulence. Heat transfer between melt and crucible, even at points of contact, can be minimised, if turbulent diffusion is suppressed. A well-known technique for suppressing turbulence in a conducting fluid is through the application of a DC magnetic field. In a hypothetical scenario, a secondary DC coil, carrying 10kAmps was added below the original AC coil. The general arrangement is shown in Figure 11.

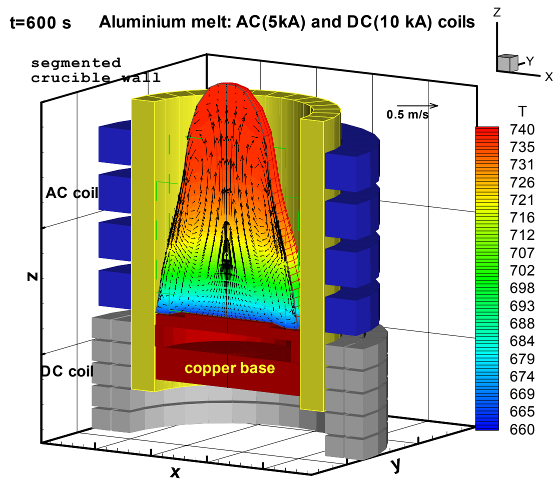

Figure 11: Arrangement with DC coil placed below the AC induction coil – Superheat increases to 740^{o}C

Switching the DC field on once the metal is in a molten state, indeed led to an increase in maximum superheat for Al from 680^{o}C to 740^{o}C! This increase can be seen in Figure 12. In addition the DC field leads to a substantial damping of the free surface oscillations which can also be seen in the base and finger power traces in Figure 12. The same technique will increase superheat in Ti melts, but to a lesser extent, due to the difference in electrical conductivity between the two metals.

The damping of turbulence (and also the mean convection) can be seen more directly in Figures 13 (a) and (b) which contrast the fields of turbulent kinetic energy between the two simulations. The bulk of the flow is highly turbulent in 13(a), but only the fast-moving skin layer in 13(b).

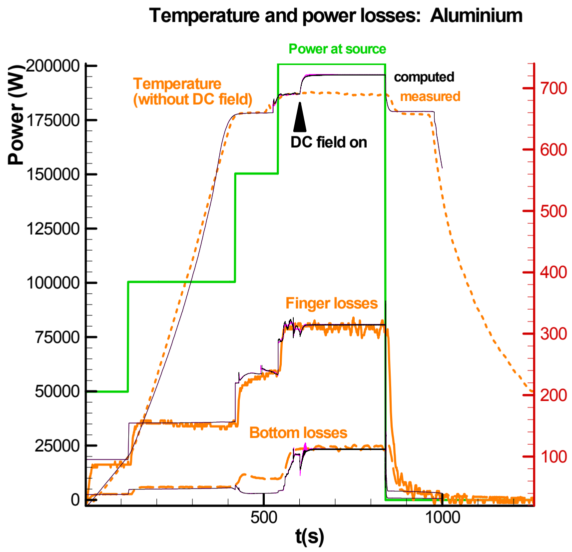

Figure 12: DC field on at 600s – note increase in melt

Other parameters such as the supply frequency, size and dimensions of the load, relative position of the coil(s), base geometry were also investigated using this model. Space does not permit us to include more results here, although some of these have been included in the references.

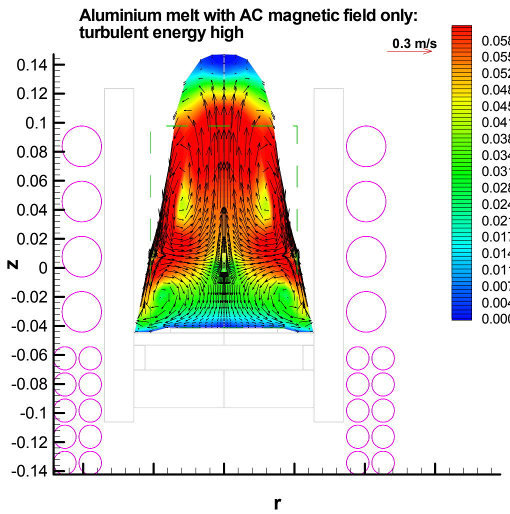

Figure 13 (a): No DC field - High turbulence levels maintained throughout the melt (k-max=0.0588)

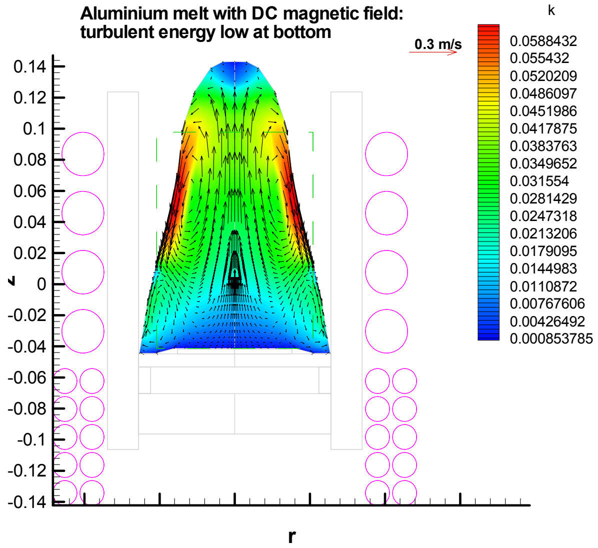

Figure 13 (b): DC field on- Both turbulence and mean advection damped. High turbulence remains close to the side free surface (k-max=0.0588)

CONCLUSIONS

This paper presented some aspects of a lengthy, in-depth study of the ISM cold-crucible melting process. The emphasis here has been on the development and validation of a useful numerical model of the process, which is based mainly on a pseudo-spectral technique. A series of experiments designed to assist the modelling effort were also described. The conclusions of this study can be summarised as follows:

- The different materials exhibit distinctive melting sequence characteristics. Modelling gives an insight to the physical events in the process and provides clues on how to improve it.
- Attention is focussed into maximising superheat, important for the casting of thin-sections such as turbine blades.
- It is shown that the introduction of an additional DC field reduces heat losses to the water-cooled crucible walls by damping bulk turbulence and also maximises Joule heating by stabilizing the liquid surface.
- The copper crucible coolant temperatures may be used to estimate heat losses and to validate the numerical simulation.
- The molten material acquires a dome shape and the observed dome height may also be used as a validation parameter, revealing a strong link between the level of confinement and thermal efficiency.

REFERENCES

1. NODA, T., "Application of cast gamma TiAl for automobiles", Intermetallics, 6 (1998) 709-713.
2. BLUM, M. ET AL., "Commissioning of a prototype plant for the economical mass production of TiAl valves", Structural Intermetallics 2001, ed. K J Hemker et al. (Warrendale, TMS, 2001), 131-135.

3. HARDING, R.A., WICKINS, M. and LI, Y.G., “Progress towards the production of high quality γ-TiAl castings”, Structural Intermetallics 2001, ed. K J Hemker et al. (Warrendale, TMS, 2001), 181-189
4. BOJAREVICS, V., PERICLEOUS, K., “Investigation of the cold crucible melting process: experimental and numerical study” 5th Int. Conf. on Fundamental and Applied MHD, Ramatuelle, France, September 2002).
5. BOJAREVICS, V., PERICLEOUS, K., “Induction-skull melting dynamics for different materials: numerical modelling and comparisons with experiments” MCWASP X, Florida, 2003
6. CAGRAN, C. ET AL., “Thermophysical properties of a Ti-44%Al-8%Nb-1%B alloy in the solid and molten states”. (Paper presented at Thermodynamics of Alloys, Rome, 8-13 September 2002).
7. PERICLEOUS, K., Computing the dynamic interaction of magnetic fields and turbulent conducting fluids in metals processing” TMS, Seattle 2001
8. BOJAREVICS, V., PERICLEOUS, K. and CROSs, M., *Metall. Materials Trans. B*, 31B, 2000, 179-189.
9. BOJAREVICS. A., BOJAREVICS, V., GELFGAT, J. and Pericleous, K., Magnetohydrodynamics, 35, 1999, 258-277.
10. WILCOX, D.C.. Turbulence Modelling for CFD, 2nd ed., DCW Industries, California, 1998.
11. PHYSICA: www.multi-physics.com

ACKNOWLEDGMENTS

The financial assistance of the EPSRC is gratefully acknowledged in this project.